Large eddy simulation of the Cambridge/Sandia stratified flame with flamelet-generated manifolds: Effects of non-unity Lewis numbers and stretch

Weijie Zhang [a,b], Süleyman Karaca [b], Jinhua Wang [a], Zuohua Huang [a], Jeroen van Oijen [b,*]

[a] *State Key Laboratory of Multiphase Flow in Power Engineering, Xian Jiaotong University, Xian 710049, China*
[b] *Eindhoven University of Technology, PO Box 513, Eindhoven 5600 MB, the Netherlands*

ARTICLE INFO

ABSTRACT

The Cambridge/Sandia turbulent stratified flame (SwB5) is simulated with the LES and Flamelet-Generated Manifolds (FGM) combustion model. Three 3D FGM manifolds are adopted. With the purpose to examine the influence of transport properties, unity and non-unity Lewis numbers (*Le*) are included in the first two manifolds, respectively. The combined effects of non-unity *Le* and stretch are investigated in the third manifold. Heat loss to the wall is also modeled. Good agreement is found between the simulation and experiment. The equivalence ratio, temperature and mass fractions of CO and H_2 are all well reproduced in contrast with previous simulations. It is found that using non-unity *Le* can even deteriorate the near-wall temperature modeling. Non-unity *Le* is proposed to be crucial for the CO prediction as well, besides H_2. The equivalence ratio modeling is observed to be very important, which accounts for several non-unity *Le* effects. Flame stretch shows almost no impact on the velocity fields, whereas its effects on the species, equivalence ratio and temperature are identified, although to a limited extent for the Cambridge/Sandia flame.

1. Introduction

In practical devices, fuel and the oxidizer are not always mixed perfectly which leads to partially premixed or stratified flames. Stratified flames have attracted increasing interest due to their practical relevance [1]. Recently, both Masri [2] and Lipatnikov [3] reviewed the advances in partially premixed and stratified flames.

The Cambridge/Sandia burner designed by Sweeney et al. [4,5] has been widely adopted to investigate stratified flames. Due to the availability of full sets of experimental velocity, temperature, and species profiles, it is also the benchmark test case for numerical modeling. Nowadays, Large Eddy Simulation (LES) is a widely used approach for turbulent flame simulation. Various LES results on the Cambridge/Sandia burner have been reported using different combustion models [1,6–10].

The purpose of this study is to address several miss-predicted points in previous simulations, that could be caused by reduced transport properties with a unity Lewis number (*Le*) assumption. In

the Cambridge/Sandia flames, an increased equivalence ratio was experimentally measured above its bluff-body, which was rarely reproduced before by simulations [1,6]. Barlow et al. experimentally observed that this is due to preferential diffusion of H_2 and H_2O [11]. Results of Barlow et al. [11], Katta and Roquemore [12] and Turkeri et al. [1] all observed that the atomic mass fractions are not conserved through the flame brush. This indicates the vital role played by detailed transport properties with non-unity *Le* in the modeling.

Non-unity *Le* leads to preferential diffusion between species, as well as between species and heat [13]. Nevertheless, the reduced model of unity *Le* and equaled diffusivity were widely used in the literature due to a lower cost and simplicity [14,15]. Actually, although the turbulent diffusivity dominates a lot in turbulent flames, the preferential diffusion can not be ignored, considering its widely observed effects to enhance the turbulent burning velocity even with extremely strong turbulence [16,17]. The consequence of the unity *Le* assumption is inaccurate predictions of the equivalence ratio mentioned above and certain species, especially H_2 with relatively high molecular diffusivity. Note that Nambully et al. [7,8] solved mixture fraction with a source term related to the preferential diffusion effects, and the equivalence ratio was captured better. Non-unity *Le* was generally used in previous

* Corresponding author.
  E-mail address: j.a.v.oijen@tue.nl (J.v. Oijen).

detailed simulations of hydrogen flames [18–21]. However, accurate H_2 predictions were not reported in LES results of the Cambridge/Sandia flame.

One common feature of previous results is that the CO was not well predicted [1,6–8,10]. The modeled CO was much lower than the experimental results especially in the recirculation zone above the bluff-body. This discrepancy was declared to be "unclear" by Brauner et al. [10], while Nambully et al. [7,8] stated that, the tabulated chemistry adopted is probably insufficient to represent the CO solution, or the conversion to CO_2 by the increased O_2 concentration. Proch and Kempf [6] and Turkeri et al. [1], however, attributed this to the adiabatic wall boundary and thus the overprediction of temperature. Recently, Mercier et al. [22] and Mehl et al. [23] both proposed that the sub-grid scale flame surface can influence the CO prediction by using the Filtered Wrinkled Flamelets (FWF) model. In the present study, however, the non-unity Le effects on the CO prediction are mainly investigated. Actually, including detailed transport properties by using non-unity Le probably improves the CO prediction a lot, as inspired by Han et al. [24]. This needs further examination.

In turbulent flames, the local flame speed and adiabatic temperature can be modified by the stretch induced by curvature or straining of non-uniform flow [25]. The vital role played by stretch was observed by Knudsen et al. [26], van Oijen et al. [27], and recently Han et al. [24] in modeling premixed flames with high Karlovitz number. To capture the stretch effects on composition and kinetics, non-unity Le has to be included, whereas a flame with unity Le will be almost insensitive to stretch [15,28]. Stretch effects in the Cambridge/Sandia flame were not investigated before since the unity Le assumption was extensively applied.

In order to further identify the effects of detailed transport properties, the Cambridge/Sandia stratified flame is simulated with the tabulated Flamelet-Generated Manifolds (FGM) combustion model [29,30], by using both unity and non-unity Le. With non-unity Le, the stretch effects are also examined. Their influence on the velocity, temperature, species and especially the CO and H_2 predictions is discussed in detail. It is worth to be noted that even though flame stretch was included in previous studies of pure premixed flames with the FGM method [18,27,31] or other tabulated methods [24,26], its application in a stratified or partially premixed flame seems never performed before. Donini et al. [14] included non-unity Le in a stratified laminar Bunsen flame, but stretch was ignored in the flamelet calculations. Heat loss is also included in the present study, which was revealed to be vital for the prediction of near-wall temperature [1,6,9,32,33].

State-of-the-art of the FGM method was reviewed recently by van Oijen et al. [15]. The FGM and other tabulated combustion models are expected to be very useful for modeling real industry-scale burners at a low cost. The present study validates the performance of the FGM method for turbulent stratified premixed flames. The results also contribute to improving its capability to predict reliable combustion processes, near-wall temperature and pollutant species.

2. Numerical methodology

2.1. The Cambridge/Sandia stratified flame

The modeling setup is introduced here briefly. The Cambridge/Sandia burner was designed for stratified premixed swirl and non-swirl flames. The burner schematic is shown in Fig. 1, where d represents the diameter. In the present study, only the non-swirl case SwB5 is considered, which was also extensively simulated before [1,9]. One case is enough for this study to investigate the transport properties and stretch. For this case, premixed CH_4/air mixtures at different equivalence ratios of $\phi_i = 1.0$
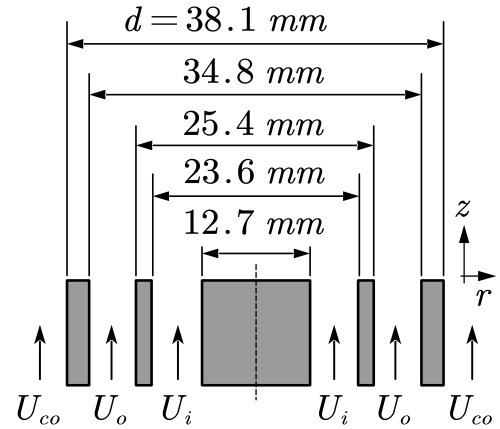

Fig. 1. A cross section view through axis of the Cambridge/Sandia burner.

and $\phi_o = 0.5$ are provided through the inner and outer tube, respectively. The equivalence ratio is defined as [4,34]:

$$\phi = \frac{(X_{H_2} + X_{H_2O})/2 + X_{CO_2} + X_{CO} + 2X_{CH_4}}{X_{O_2} + X_{CO_2} + (X_{CO} + X_{H_2O})/2} \tag{1}$$

where X_i is the mole fraction of species i.

Mean velocities of the inner and outer tube are $U_i = 8.31$ m/s and $U_o = 18.7$ m/s, respectively. Co-flow air is supplied around the outer annulus with $U_{co} = 0.4$ m/s. The flame then stabilizes above the bluff-body, where an inner recirculation zone (IRZ) is formed. Velocity measurements of the flame are provided by Zhou et al. [34], while temperature and mass fraction measurements are from Sweeney et al. [4,5]. The temperature on the bluff-body is also available to impose a non-adiabatic boundary. Note that $z = 0$ mm at the exit plane, and $r = 0$ mm at the bluff-body center.

2.2. Flamelet-generated manifold approach

2.2.1. Control variables

In finite rate chemistry models, resolving the aerodynamic motion and chemistry means that tens or even hundreds of stiff equations need to be solved, which is prohibited with the current and near future computing ability [35,36]. Chemical reduction techniques are useful to reduce the number of equations. However, they are still computational expensive compared to the tabulated combustion model such as the FGM method, where there are only several equations of Control Variable (CV) being solved [15].

The FGM model reduces the chemical model with the flamelet assumption. Based on a set of laminar flamelets for given initial conditions, a database of thermochemical variables (f) can be built and stored as a function of CVs in the pre-processing stage. Basically, the Progress Variable (PV, denoted by $\mathcal{y}$) must be included in the premixed flame as a CV, describing the transition from fresh to burned equilibrium gases. The progress variable is defined as:

$$\mathcal{y} = \sum_{i=1}^{N_s} \alpha_i Y_i \tag{2}$$

where α_i are arbitrary weighting coefficients, Y_i is the mass fraction of species i and N_s is the total number of species. The only restraint is to ensure a monotonic $\mathcal{y}$ through the flamelet. In the present study, the coefficients were defined similar to Donini et al. [36]: $\alpha_{CO_2} = 100M_{CO_2}^{-1}$, $\alpha_{H_2O} = 100M_{H_2O}^{-1}$, $\alpha_{H_2} = 100M_{H_2}^{-1}$, $\alpha_{O_2} = -100M_{O_2}^{-1}$, and $\alpha_i = 0$ for other species. M is the molecular mass of the species in g/mol.

Considering the stratification of equivalence ratio in the Cambridge/Sandia flames, and heat loss to the bluff-body, the mixture

Table 1
Three 3D FGM models adopted.

Manifolds	CV	Le	Stretch	Heat loss	Grid size
ZhPV	$Z, h, \mathcal{Y}$	Unity	No	Yes	$80 \times 200 \times 100$
ZhPV-Le	$Z, h, \mathcal{Y}$	Non-unity	No	Yes	$80 \times 200 \times 100$
ZZ2PV-Le	$Z, Z_2, \mathcal{Y}$	Non-unity	Yes	No	$80 \times 100 \times 100$

fraction (Z) and enthalpy (h) were also included. Z is defined as a function of the element mass fractions Y_j^e of elements j [15,37]:

$$Z = \frac{0.5M_H^{-1}\left(Y_H^e - Y_{H,2}^e\right) + 2M_C^{-1}\left(Y_C^e - Y_{C,2}^e\right) - M_O^{-1}\left(Y_O^e - Y_{O,2}^e\right)}{0.5M_H^{-1}\left(Y_{H,1}^e - Y_{H,2}^e\right) + 2M_C^{-1}\left(Y_{C,1}^e - Y_{C,2}^e\right) - M_O^{-1}\left(Y_{O,1}^e - Y_{O,2}^e\right)} \tag{3}$$

The subscripts 1 and 2 represent pure fuel and oxidizer, respectively. The specific enthalpy was adopted as a CV to describe the energy [30]:

$$h = \sum_{i=1}^{N_s} Y_i h_i \tag{4}$$

with

$$h_i = h_i^{ref} + \int_{T^{ref}}^{T} c_{pi}(T') dT' \tag{5}$$

where h_i^{ref} is the enthalpy of formation at reference temperature T^{ref} (300 K in this study) and c_{pi} is the specific heat capacity at constant pressure of species i.

With non-unity Le, the flame is sensitive to stretch [15,18]. It is well known that their combined effect results in a redistribution of element mass fraction of C, H, O, N, and enthalpy. Theoretically, at least three elements and the enthalpy must be solved [25]. However, previous studies showed that extending the FGM with only one CV, for example a combination of two element mass fractions, can be sufficient [15,18,28]. Therefore, another mixture fraction Z_2 was adopted as a CV for stretch effects in this study:

$$Z_2 = 0.1 Y_O^e + Y_H^e \tag{6}$$

For the stretched flamelets, another progress variable was used with the following coefficients in Eq. (2): $\alpha_{CO_2} = 100 M_{CO_2}^{-1}$, $\alpha_{H_2O} = 100 M_{H_2O}^{-1}$, and $\alpha_i = 0$ for other species, in order to avoid crossing of flamelets in the CV space [31].

2.2.2. FGM tabulation

Three 3D manifolds were used, as shown in Table 1. The first two manifolds ZhPV and ZhPV-Le both include mixture fraction for fuel stratification, enthalpy for heat loss and progress variable. Unity and non-unity Le were applied to the two manifolds (namely, to the diffusion term of the laminar flame solution), respectively. The manifold of ZZ2PV-Le includes non-unity Le and stretch, while the heat loss is neglected. It is a challenge to include both the heat loss and stretch in ZZ2PV-Le, which leads to a 4D manifold. One reason is that there will be too many stretched laminar flamelets to be computed at each mixture fraction and heat loss level. Another reason is that, as mentioned before, to account for the stretch effects, non-unity Le must be adopted. The non-unity Le will result in curvilinear grid of CVs in the manifold (as will be shown below), and will be difficult for data retrieving if the manifold possesses a higher dimension.

Laminar flamelets were solved for different values of equivalence ratio to include the mixture fraction as a CV. The range goes from $\phi = 0.5$, which is close to the flammability limit, to $\phi=1.20$ (higher than ϕ_i). Meanwhile, the mixture fraction needs to be extrapolated to zero from the lean limit, so as to model the co-flow

air. Flamelet solutions were computed with the 1D flame code Chem1D [38]. GRI-Mech 3.0 was adopted, which consists of 325 elementary reactions and 53 species [39].

The flamelets were solved with inlet/unburned temperature of $T_u=300$ K. To model the heat loss, at each equivalence ratio, a set of laminar flamelets were solved for different values of enthalpy h. This was performed by computing the burner-stabilized flames at a constant ϕ [29,36,40]. Furthermore, preheated flamelets with $T_u=300–600$ K were also included to allow preheating of the mixture.

To take stretch effects into account in manifold ZZ2PV-Le, a set of stretched flamelets was solved at each equivalence ratio. Basically, a stretched flamelet can be obtained by a counter-flow model, as adopted in [24,26]. In Chem1D, however, a stretch rate (K) can be imposed directly in the 1D laminar flamelet equations [29], which is the method used in this study. A broad range of negative and positive K was imposed until the solution diverges at a near-extinction condition. A different way is to apply curvature-induced stretch to the flamelet. Previous studies have shown that how the stretch is modeled has little effect [25,27].

With these flamelet solutions, the thermochemical variables were mapped as a function of the CVs. The FGM tabulation was completed by storing all the variables to a tridimensional grid defined by the CVs in Table 1. The number of the grid points is also shown in the table.

Sample slices of the manifolds with a constant equivalence ratio $\phi = 1.0$ are displayed in Fig. 2. In these figures, only a part of the flamelets are shown sparsely. It is seen that with unity Le, the enthalpy is constant along the progress variable of a flamelet in Fig. 2a. Note that $\Delta h = h - h_a$, and h_a is the enthalpy of adiabatic flamelets with $T_u=300$ K. With non-unity Le in ZhPV-Le, the enthalpy now is redistributed in Fig. 2b. In Fig. 2c, the non-unity Le and stretch result in varied element mass fraction along the flamelet.

However, the curvilinear grid of CVs in Fig. 2b and c brings difficulty to data retrieving during the computation. Comparatively, the rectilinear grid in Fig. 2b is much easier to use. One useful method is to regrid the curvilinear table to a structured mesh and using multi-dimensional linear interpolation for retrieval [15]. In the present study, rectilinear meshes were also used for manifolds ZhPV-Le and ZZ2PV-Le. The rectilineared results are demonstrated in Fig. 3. Note that the obtained mesh lines are not real laminar flamelets, but it will not hinder the computation. For ZZ2PV-Le, the CVs $\mathcal{Y}$ and Z_2 were permuted before the curvilinear-to-rectilinear conversion. The chemical source of $\mathcal{Y}$ is shown in Fig. 3. In Fig. 3, the increase of stretch leads to a decreasing Z_2 and $\mathcal{Y}$ source. The curvilinear-to-rectilinear conversion is performed for a maximum of 3D manifold in this study. One problem is that, for manifolds with higher dimension, it will be much more difficult. New methods for data storage and retrieving remain to be extensively developed [15].

2.2.3. LES filtered governing equations

Besides the continuity and momentum equations, transport equations for the CVs were solved in the FGM combustion solver. For a N_{cv}-dimensional FGM with multiple CVs, thermochemical variables $f = f(C_1, C_2, \ldots, C_{N_{cv}})$ were retrieved from the tabulated manifold. The LES filtered equations of C_k can be written as [14,15]:

$$\frac{\partial \hat{\rho}\tilde{C}_k}{\partial t} + \nabla \cdot \left(\hat{\rho}\tilde{\mathbf{u}}\tilde{C}_k\right) - \nabla \cdot \left\{ \left[\widehat{\left(\frac{\lambda}{c_p}\right)} + \frac{\mu_t}{Sc_t} \right] \nabla \tilde{C}_k \right\}$$
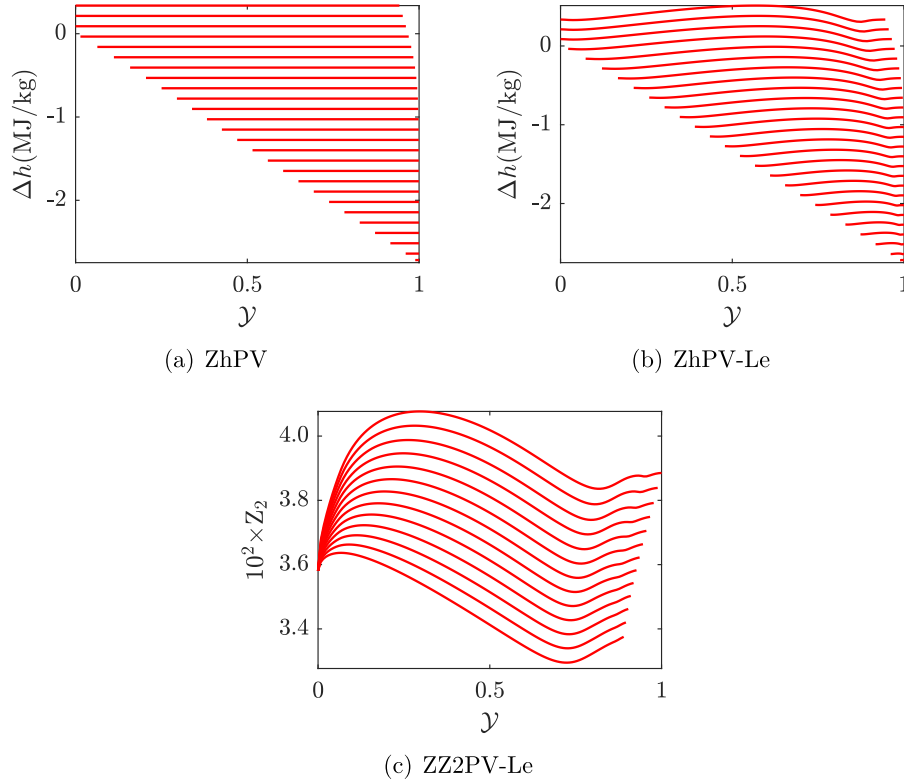$$= \nabla \cdot \left(\hat{d}_{C_k} \nabla \tilde{y}\right) + \hat{\omega}_{C_k} \tag{7}$$

(a) ZhPV

(b) ZhPV-Le

(c) ZZ2PV-Le

Fig. 2. Sample FGM table slices at constant $\phi = 1.0$.
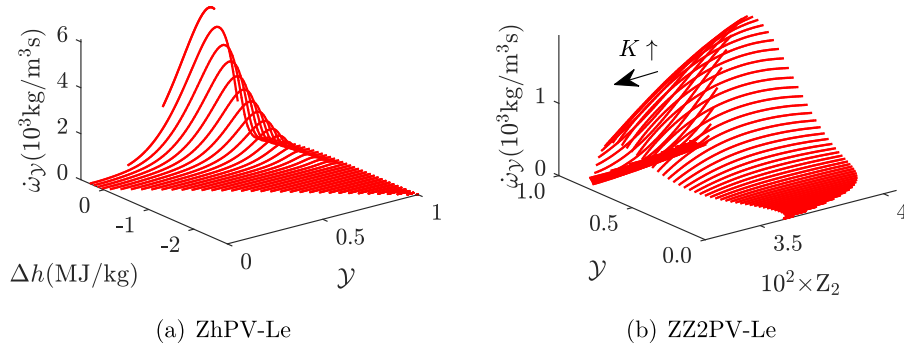

(a) ZhPV-Le

(b) ZZ2PV-Le

Fig. 3. Rectilineared FGM table slices at constant $\phi = 1.0$.

in which $\hat{q}$ denotes a spatially filtered quantity and $\tilde{q} = \frac{\widehat{\rho q}}{\bar{\rho}}$ a spatially Favre filtered quantity. ρ is the density, λ the heat conductivity and c_p the mixture specific heat capacity. The thermodynamic coefficients are computed with a mixture-averaged approach and stored in the manifolds, see [41] for a detailed description. μ_t is the turbulent eddy viscosity and Sc_t is the turbulent Schmidt number, which is assumed to be a constant of 0.7 [36]. The source term of $\dot{\omega}_{C_k}$ is nonzero only for $\mathcal{Y}$ in the present study.

The first term on the R.H.S. of Eq. (7) is the preferential diffusion term induced by non-unity Le. For the 3D manifolds in this study, the diffusion coefficients are (assuming $C_1 = \mathcal{Y}$) [14]:

$$d_{C_1} = \frac{\lambda}{c_p} \sum_{i=1}^{N_s} \left[D_{1,i} \left(\frac{1}{Le_i} - 1 \right) \left(\frac{\partial Y_i}{\partial \mathcal{Y}} + \frac{\partial Y_i}{\partial C_2} \frac{\partial C_2^{1D}}{\partial \mathcal{Y}} + \frac{\partial Y_i}{\partial C_3} \frac{\partial C_3^{1D}}{\partial \mathcal{Y}} \right) \right] \quad (8)$$

$$d_{C_2} = \frac{\lambda}{c_p} \sum_{i=1}^{N_s} \left[D_{2,i} \left(\frac{1}{Le_i} - 1 \right) \left(\frac{\partial Y_i}{\partial \mathcal{Y}} + \frac{\partial Y_i}{\partial C_2} \frac{\partial C_2^{1D}}{\partial \mathcal{Y}} + \frac{\partial Y_i}{\partial C_3} \frac{\partial C_3^{1D}}{\partial \mathcal{Y}} \right) \right] \quad (9)$$

$$d_{C_3} = \frac{\lambda}{c_p} \sum_{i=1}^{N_s} \left[D_{3,i} \left(\frac{1}{Le_i} - 1 \right) \left(\frac{\partial Y_i}{\partial \mathcal{Y}} + \frac{\partial Y_i}{\partial C_2} \frac{\partial C_2^{1D}}{\partial \mathcal{Y}} + \frac{\partial Y_i}{\partial C_3} \frac{\partial C_3^{1D}}{\partial \mathcal{Y}} \right) \right] \quad (10)$$

These coefficients are computed in the pre-processing stage and stored in the manifold. Note that Eqs. (7) to (10) are derived based on the assumption that, locally the CV of C_k is a function of $\mathcal{Y}$ solely [14,15,31]. Accordingly, the term of $\frac{\partial C_k^{1D}}{\partial \mathcal{Y}} \approx \frac{dC_k^{1D}}{d\mathcal{Y}}$ can be computed directly in the 1D flamelet. Le_i is the Lewis number of species i. If the unity Le assumption is adopted, $Le_i = 1$ and $d_{C_k} = 0$, indicating no preferential diffusion effects. The coefficient $D_{k,i}$ equals α_i for $\mathcal{Y}$ Eq. (2)), and equals h_i for enthalpy (Eq. (4)). For mixture fraction Z or Z_2, it is obtained by converting Eq. (3) or Eq. (6) to a similar form of Eqs. (2) and ((4).

2.2.4. Sub-filter closure

The Smagorinsky model was adopted for the sub-grid scale (SGS) turbulence and the eddy-viscosity μ_t. We have examined that other turbulence models improve the present results to a
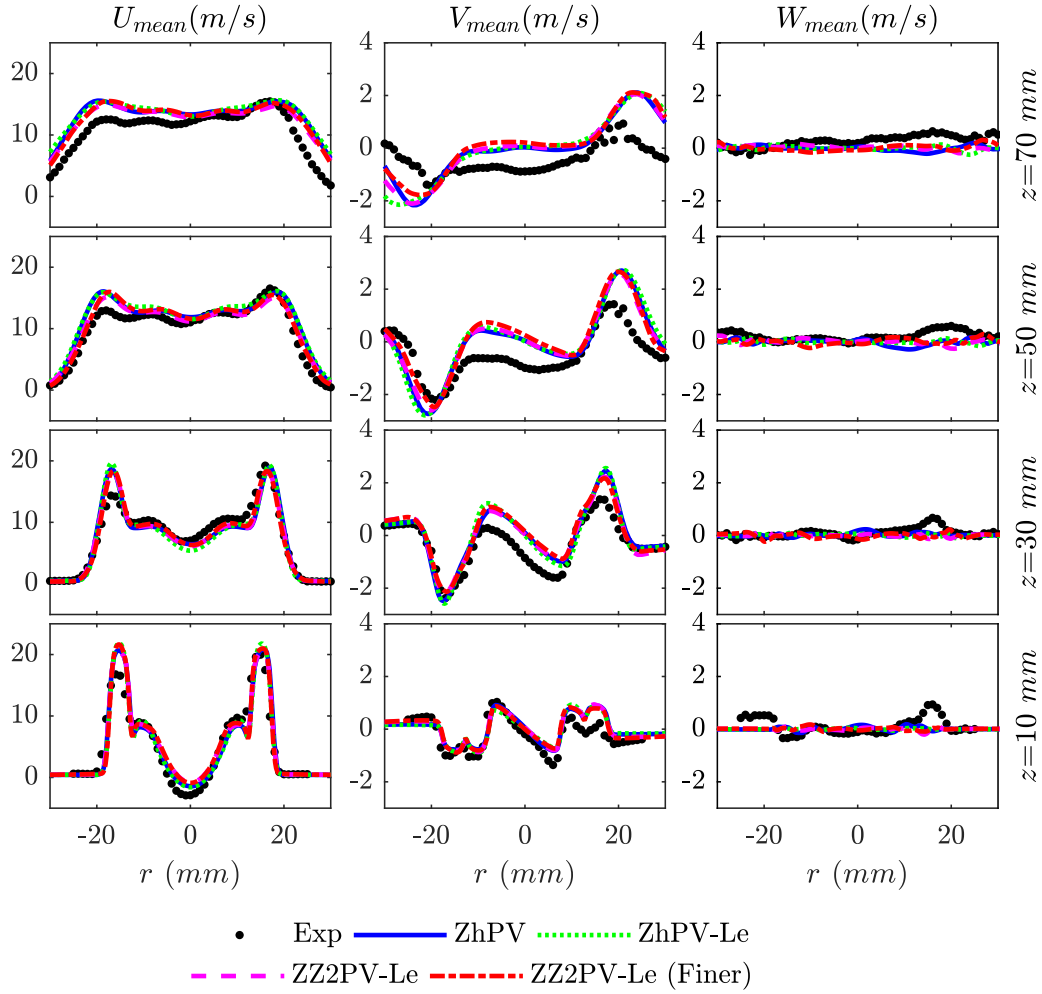
Fig. 4. Radial profiles of the mean velocity at different axial locations.

quite limited extent; therefore, this classical model was ultimately used mainly for its simplicity. To account for the unknown sub-filter term of the thermochemical variables, the presumed β-pdf approach has been widely used [6,26,36,42]. The disadvantage is that the FGM manifold has to be extended with new dimensions of the SGS variance. In the present study, an alternative top-hat function model was used, as proposed by Floyd et al. [43]. There is no need to extend the database dimension with this model.

Following Proch et al. [6], the sub-filter variations of mixture fraction (as well as Z_2) were ignored. The mixture fraction Z was observed to vary in a quite limited range within the mesh cell even in their coarse mesh (mesh size Δ=1 mm) for the Cambridge/Sandia flame. Meanwhile, similar to Donini et al. [36], the variance of enthalpy was also ignored due to its rather modest gradients and fluctuations. Therefore, the top-hat model was only implemented for $\mathcal{Y}$. The SGS variance was computed with an algebraic model with $C_v = 1/12$ [36,43–45]:

$$\widetilde{y''^2} = C_v \Delta^2 \frac{\partial \tilde{y}}{\partial x_i} \frac{\partial \tilde{y}}{\partial x_i} \tag{11}$$

The top-hat function was then obtained as [43]:

$$p(\mathcal{Y}) = \begin{cases} \frac{1}{b-a}, & a \leqslant \mathcal{Y} \leqslant b \\ 0, & \mathcal{Y} < a \text{ or } \mathcal{Y} > b \end{cases} \tag{12}$$

where $a = \tilde{y} - \frac{1}{2}\sqrt{12\widetilde{y''^2}}$ and $b = \tilde{y} + \frac{1}{2}\sqrt{12\widetilde{y''^2}}$. Finally, with the 3D manifolds shown in Table 1, the low-pass filtered quantity f

was computed by:

$$\hat{f} = \int_{-\infty}^{+\infty} p(\mathcal{Y})f(C_1 = \mathcal{Y}, C_2, C_3)\mathrm{d}\mathcal{Y} \tag{13}$$

in which C_2 and C_3 can be Z, Z_2 or h. Though the integration can be included in the tabulation stage [45], it was implemented on-the-fly in the present study. Note that besides the presumed pdf model, the artificially thickened flame model can be combined with the FGM to account for the SGS terms [6]. The filtered flamelet model such as the F-TACLES developed by Fiorina et al. [46], is also a good choice.

2.3. Numerical setup

The computational domain spans 160 mm in the axial z direction from the burner exit, and 200 mm in the radial r direction with the model shown in Fig. 1. Hexahedral meshes with two kinds of resolution were used. The number of cells of the coarse one is about 2.6 million with cell size $\Delta < 0.73$ mm within the core region of $r < 20$ mm, and the finer mesh possesses about 6.5 million cells, with $\Delta < 0.53$ mm in the core region. The refinement is quite moderate. Even though, the simulated results are satisfactory as will be shown below when compared against the experimental results. This is primarily because, the maximum cell size in the core region is actually very equivalent to the laminar flame thickness, especially in the upstream region, and the flamelet is expected to be largely resolved. Note that the laminar flame thick-
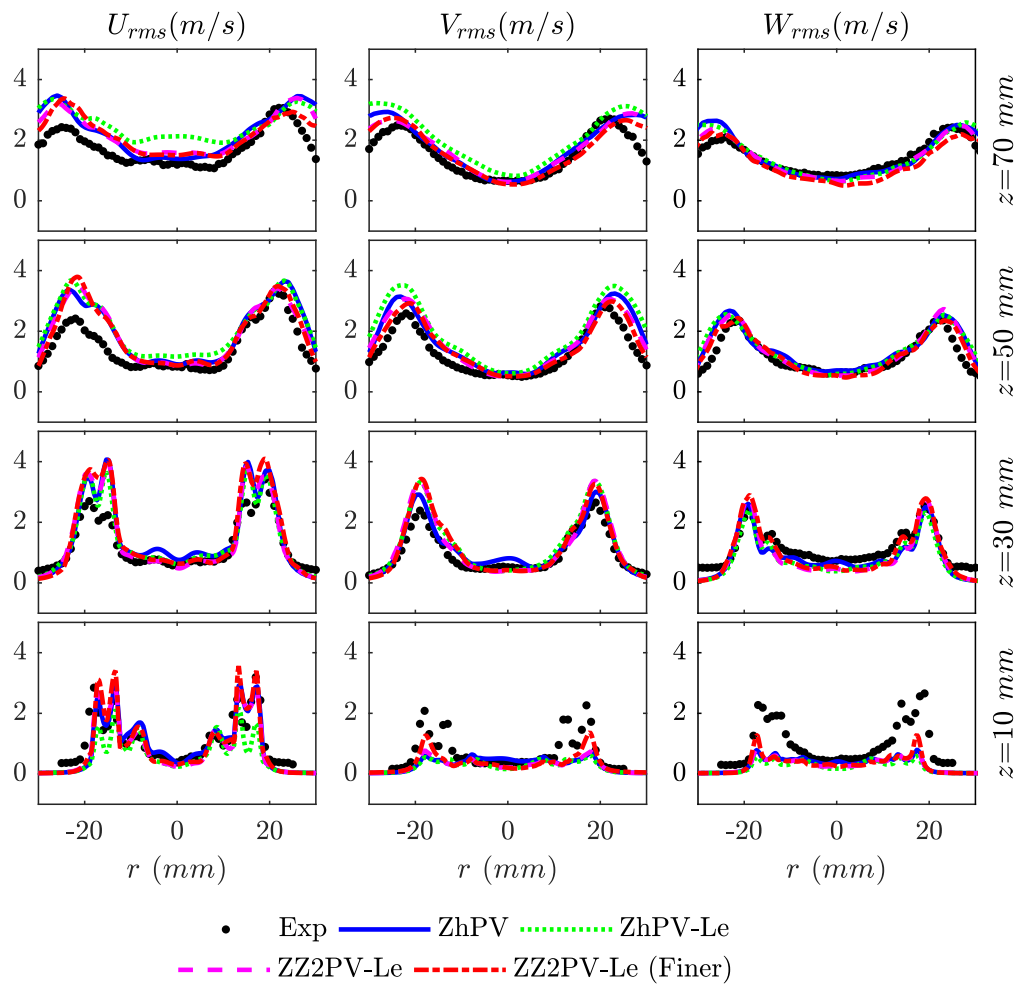
Fig. 5. Radial profiles of the rms velocity at different axial locations.

ness is about 0.51 mm for the CH_4/air flame at $\phi = 1.0$, following the definition of $(T_{\max} - T_{\min})/(\frac{dT}{dx})_{\max}$.

The inlet patch was extended 60 mm upstream from the burner exit plane to produce better tube-developed turbulence [7,10]. The inlet mean velocity profiles were tuned to match the experimental results obtained at $z = 2$ mm. Turbulent fluctuations were generated with the filtered noise method of Klein et al. [47,48]. The integral scale and turbulence intensity were set with the experimental results [34]. A non-adiabatic boundary was imposed on the bluff-body wall by setting a fixed temperature field, see [9]. A non-reflecting boundary was applied for the outlet patch.

The combustion solver was implemented in OpenFOAM. Gauss's theorem was applied for discretization. The convection and diffusion terms were discretized by second order total variation diminishing (TVD) scheme Gauss limitedLinear, and central differencing Gauss linear corrected, respectively. Limiters were adopted to make sure that the scalars are bounded. The first order implicit Euler scheme was used for temporal discretization. The pressure-velocity coupling was solved with the PISO method. The numerical diffusion may be inevitable, which can influence the relatively subtle preferential diffusion effects in the turbulent flames. However, since we compared the cases with unity/non-unity Le by using the same numerical setup, the different results obtained can highlight the Le effects.

The maximum Courant number was kept less than 0.4 with a time step of about 4×10^{-6} s. Three cases with the FGM manifolds in Fig. 1 were computed. Each simulation was firstly proceeded for 10 flow-through times (about 0.26 s) after ignition, and another 10

flow-through times for statistics. The computation was parallelized with 160 processors. For each case on the coarse mesh, the simulation was completed with approximately 27 h clock time. With a mapped initial condition from the coarse mesh, the computation on the finer mesh was firstly performed for about 0.02 s, then another 5 flow-through times to get the statistics. The clock time needed was about 37 h.

3. Results and discussion

3.1. Velocities

The resolved mean and root-mean-square (rms) velocities are shown in Fig. 4 and Fig. 5, respectively. U is the axial velocity, V the radial and W the tangential velocity. Four cases are shown with ZhPV, ZhPV-Le and ZZ2PV-Le on the coarse mesh as well as the result of ZZ2PV-Le on the finer mesh.

In Fig. 4, the mean velocities correspond well with the experimental results. However, the radial velocity deviates at higher z. At the centerline when $r = 0$, zero radial velocity is predicted by the simulation, whereas negative velocity is measured in the experiment. Proch et al. [6] also noted this and suggested that the experimental result is slightly asymmetric, which can be due to measurement uncertainties or deviations in the geometrical shape of the burner.

The rms velocities are well reproduced by the simulations except for lower V_{rms} and W_{rms} predictions at $z = 10$ mm. Probably the mesh is not fine enough to resolve the turbulence fluctuation
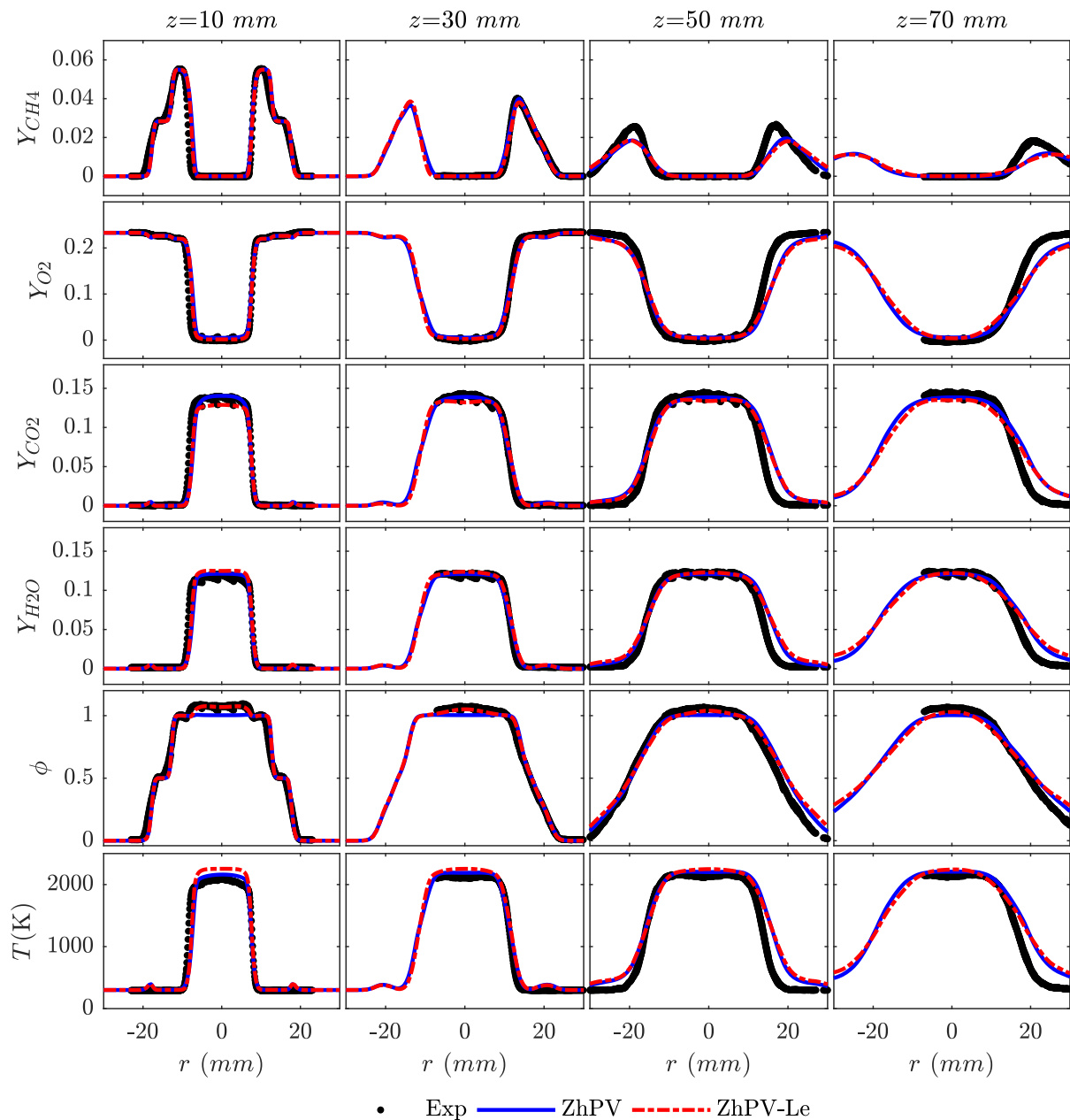
Fig. 6. Comparison of mean scalar profiles with unity and non-unity *Le*.

in the radial direction. It can also be influenced by the inlet turbulence. Anyway, it is not easy to fully replicate the experimentally measured turbulence. Further downstream, there are deviations of U_{rms} and V_{rms}. Meanwhile, the mean velocities downstream are also more deviated. Probably the interactions between the turbulent shear layer and the flame are more intensive downstream, which leads to larger unresolved sub-grid terms and deviations in the predictions [7]. Note that in the downstream region, the flame front expands outwardly (as can be seen from Fig. 8 below) whereas the hexahedral mesh quality is decreased with larger |r|; therefore, deviations are always more evident there.

With the finer mesh, the rms velocities are only slightly improved while the mean velocities are nearly not improved. Since the improvement is very limited, the computation on the finer mesh was not performed for the other two cases of ZhPV and ZhPV-Le. Note that an even finer mesh with $\Delta = 0.25$ mm and 103.2 million grid cells was adopted by Proch et al., but similar deviations were still observed [6].

From Figs. 4 and 5, it can be concluded that the Lewis number and stretch effects have little influence on the velocity statistics. The case of ZhPV-Le predicts slightly deviating velocity fluctuations in Fig. 5. This may be explained by the higher temperature predicted with non-unity *Le*, as demonstrated below.

3.2. Species, equivalence ratio and temperature

To investigate the non-unity *Le* effects, time-averaged species mass fraction (Y), equivalence ratio (ϕ) and temperature (T) of cases ZhPV and ZhPV-Le are compared in Fig. 6. Unity and non-unity *Le* are applied to the two cases, which denotes reduced and detailed transport properties, respectively. Note that ϕ is defined by Eq. (1) both in the experiment and simulation.

Both the results are in reasonable agreement with the experiment. However, in the downstream region (see $z = 50$ and 70 mm), the mass fractions of CH_4 and O_2 are predicted lower, while the
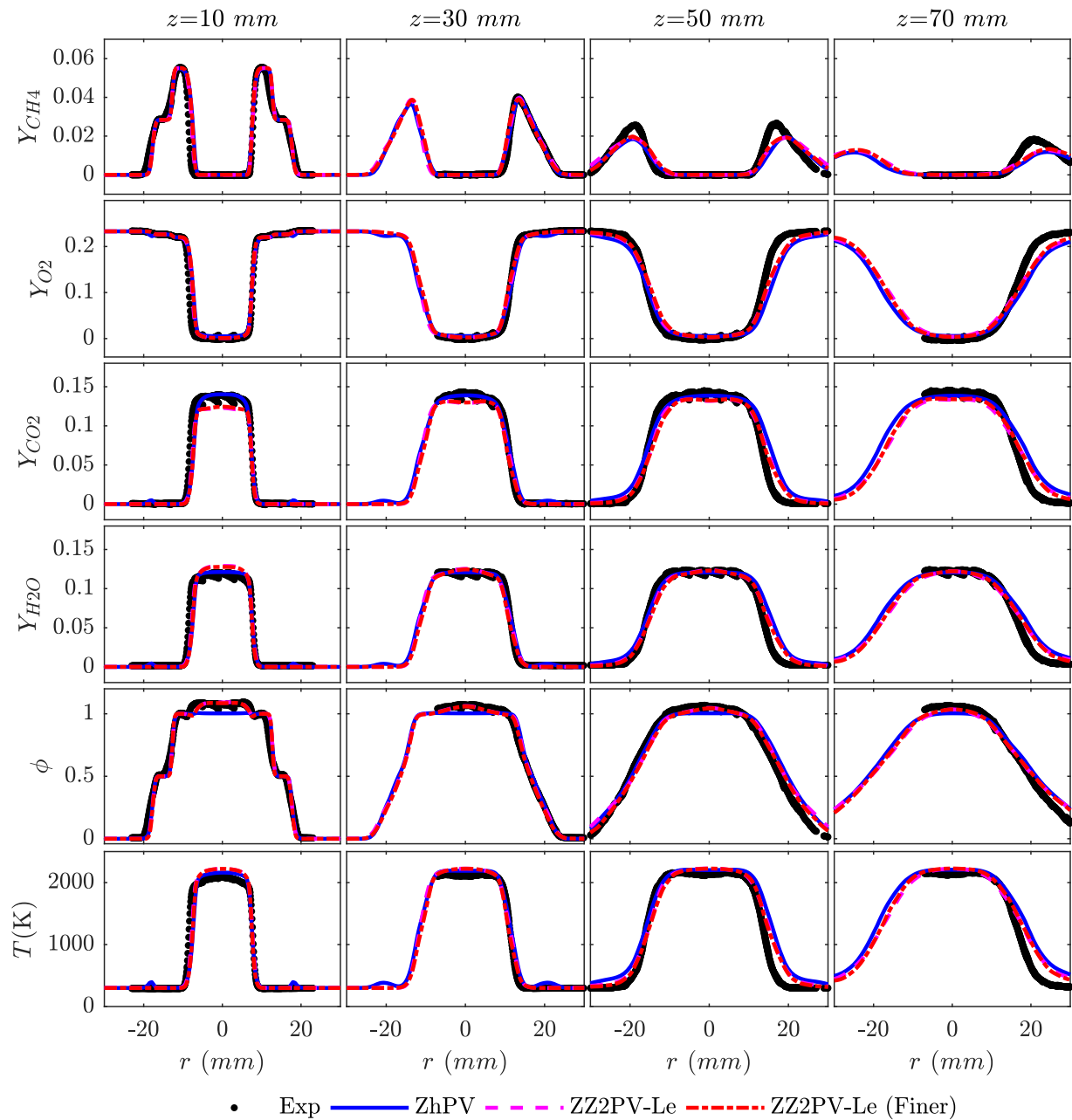
Fig. 7. Mean scalar profiles influenced by non-unity *Le* and stretch.

products of CO_2 and H_2O as well as the temperature are predicted higher. This may result from the over-predicted progress variable $\mathcal{Y}$ [26]. The top-hat SGS model was applied only for $\mathcal{Y}$, and probably the source term of $\mathcal{Y}$ was over-predicted. This can be evident downstream, since as mentioned, around the outwardly expanded flame front there, the mesh quality is decreased. Meanwhile, note that the asymmetric error from experimental measurement is still observed at $z = 50$ mm. The left side of the plots shows better agreement.

Overall, the non-unity *Le* shows no significant impact on the scalars in Fig. 6 except for in the upstream region, see profiles at $z = 10$ mm. In the case of ZhPV, the temperature at $z = 10$ mm is well modeled with heat loss. However, the equivalence ratio is under-predicted. This was observed before and can be attributed to the unity *Le* assumption [1,6]. Comparatively, the non-unity *Le* included in ZhPV-Le results in more accurate ϕ. Therefore, detailed transport properties should be vital for the ϕ prediction. But at

the same time, the temperature at $z = 10$ mm is over predicted, which should be a consequence of the higher ϕ. In spite of the non-adiabatic wall boundary, the simulated heat loss seems insufficient to compensate the over-predicted temperature. Additionally, CO_2 and H_2O are slightly under and over-predicted near the centerline, respectively.

Mean scalar profiles obtained from the ZZ2PV-Le case with non-unity *Le* and stretch are shown in Fig. 7. Both results on the coarse and finer mesh are displayed, as well as the result of case ZhPV for reference. The mesh refinement has little effect on the results. Similar deviations in the downstream region persist for major species and temperature. Note that the deviations are mitigated with inclusion of stretch effects in ZZ2PV-Le, although slightly. Similar to the case of ZhPV-Le in Fig. 6, ϕ is well predicted and the temperature is over-predicted at $z = 10$ mm in Fig. 7. The deviations of CO_2 and H_2O at $z = 10$ mm also appear and are even more apparent with stretch.
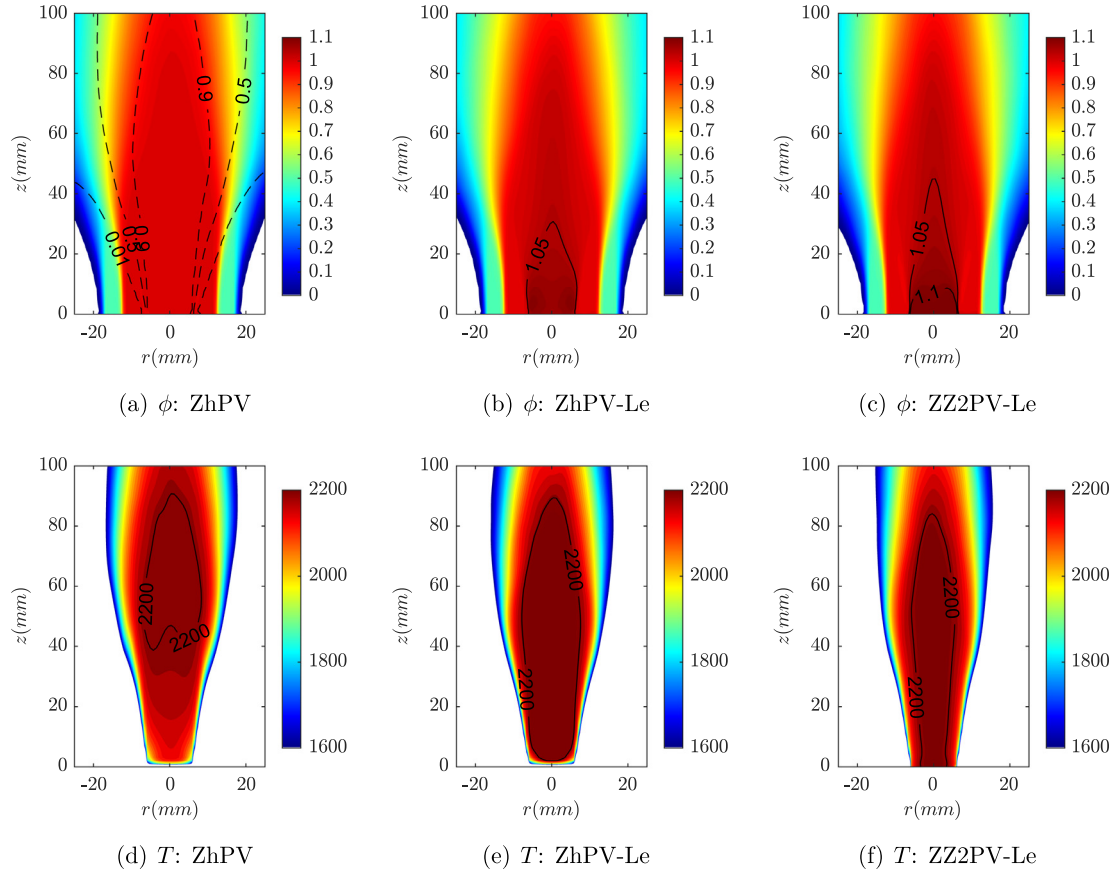
Fig. 8. Time-averaged equivalence ratio and temperature fields. The dashed line is the $\mathcal{Y}$ contour and bold line represents the ϕ or T contours.

Figure 8 demonstrates the time-averaged fields of ϕ and temperature. With non-unity Le, ϕ is increased and higher than $\phi_i = 1.0$ especially in the IRZ above the bluff-body. From Fig. 8e to f, the near-wall temperature of ZhPV is much lower in contrast with the two cases with non-unity Le. For the case of ZhPV-Le, despite of the non-adiabatic wall boundary, the higher ϕ overpowers the heat loss to the bluff-body. This leads to an apparent over-predicted temperature in the IRZ, as also reflected in Fig. 6 at $z = 10$ mm. The high temperature could be the reason for deviating rms velocities observed in Fig. 5. The flow is less turbulent upstream due to increased viscous dissipation, whereas the downstream velocity can be influenced by the thermal expansion with high temperature. The influence of temperature on the flow was also observed in [7,26].

In Fig. 8, with stretch effects in the case of ZZ2PV-Le, ϕ is predicted higher compared to ZhPV-Le. However, the near-wall temperature is reproduced better. As can be seen from the temperature profiles at $z = 10$ mm in Figs. 6 and 7, case ZZ2PV-Le predicts a lower temperature that is closer to the experimental result compared to ZhPV-Le even without heat loss. With stretch, the predicted temperature is also lower downstream, as can be seen from Fig. 8. The temperature profiles at larger z in Fig. 7 are also slightly improved. If heat loss would be included in ZZ2PV-Le, the prediction is expected to be even better. Based on these results, it can be noted that using the non-unity Le merely deteriorates the near-wall temperature prediction even with heat loss to the wall. Comparatively, the inclusion of non-unity Le and stretch predicts temperature better overall, even without heat loss.

The non-unity Le results in under-predicted CO_2 and over-predicted H_2O in the IRZ, as observed in Figs. 6 and 7. For the case of ZhPV with unity Le, the two species are even predicted better.

The underlying reason should also be the increased ϕ with preferential diffusion effects. Burned equilibrium mixture resides in the IRZ, as can be seen from the $\mathcal{Y}$ contours in Fig. 8. The equilibrium mass fractions of CO_2 and H_2O versus ϕ are displayed in Fig. 9, which are extracted at the maximum $\mathcal{Y}$ from the adiabatic laminar flamelets (300 K, see Appendix A). It is seen that Le shows no direct effect on the equilibrium mass fractions. Instead, the augmented $\phi > 1$ decreases CO_2 and increases H_2O, which correlates well with the trend in Figs. 6 and 7 for the simulations. The larger deviations of CO_2 and H_2O in case ZZ2PV-Le result from the higher ϕ with stretch effects as shown in Fig. 8c.

Since rms results of these scalars are less relevant, they are not discussed here and shown in Appendix B.

3.3. Results of CO and H_2

CO and H_2 were not well predicted in previous studies. In the present study, detailed transport properties are adopted by using non-unity Le, and the influence on CO and H_2 predictions is examined. Firstly, the CO mass fraction from case ZhPV with unity Le is displayed in Fig. 10. Similar to Donini et al. [36], a transport equation was also solved for CO within the case of ZhPV. The transport equation is written as:

$$\frac{\partial \hat{\rho} \tilde{Y}_{CO}}{\partial t} + \nabla \cdot \left(\hat{\rho} \tilde{\mathbf{u}} \tilde{Y}_{CO} \right) - \nabla \cdot \left\{ \left[\widehat{\left(\frac{\lambda}{c_p} \right)} + \frac{\mu_t}{Sc_t} \right] \nabla \tilde{Y}_{CO} \right\}$$

$$= \hat{\omega}_{CO}^p + \left(\widehat{\frac{\omega_{CO}^c}{Y_{CO}^{tab}}} \right) \tilde{Y}_{CO} \tag{14}$$
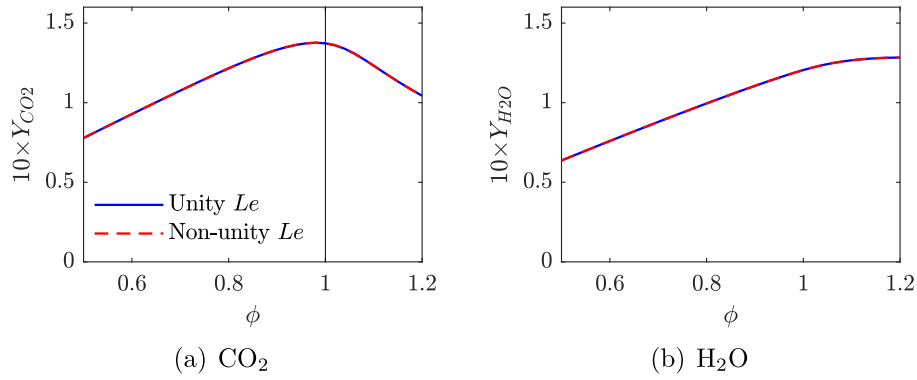
Fig. 9. Influence of *Le* and ϕ on the equilibrium mass fractions of CO_2 and H_2O.
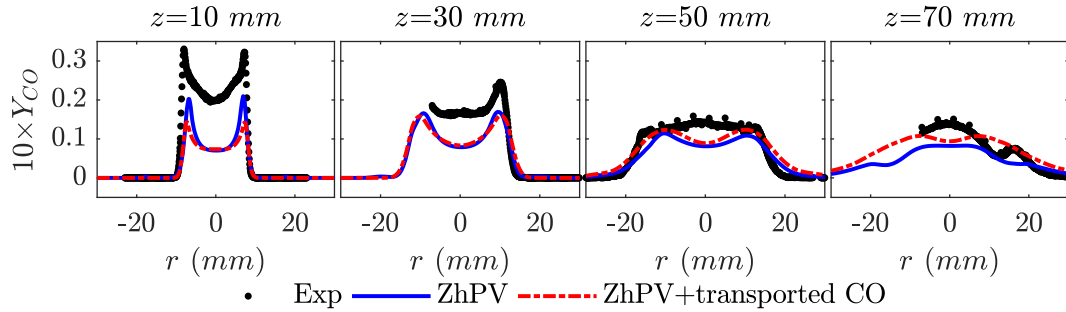

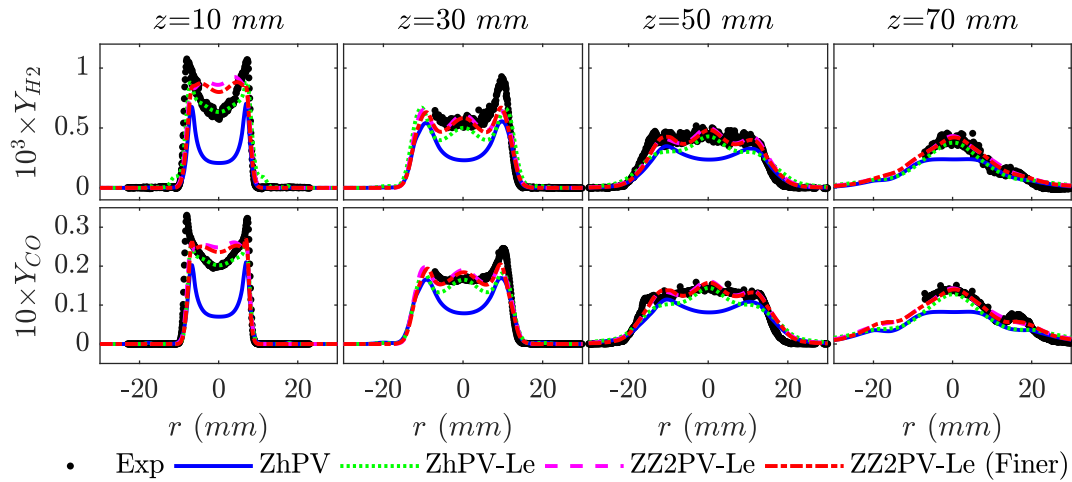**Fig. 10.** Tabulated and transported CO mass fraction with unity *Le*.

Fig. 11. Results of CO and H_2 mass fraction with non-unity *Le*.

in which there is no preferential diffusion term with unity *Le*. Meanwhile, the source of CO was split into a production ($\dot{\omega}_{CO}^p$) and a consumption ($\dot{\omega}_{CO}^c$) term, in order to compute an adaptive source term according to the local CO concentration in the LES. Y_{CO}^{tab} and Y_{CO} denote the tabulated and transported mass fraction of CO, respectively. More details can be found in Ref. [49].

The numerical results of CO in Fig. 10 obviously deviate from the experimental results. Nearly no improvements can be observed with the transported CO. Only further downstream, the transported CO gives slightly better results. With unity *Le*, the CO is underpredicted upstream (see $z = 10$ mm), which is identical to several previous results [1,6–8,10], as well as the result of Donini et al. [36].

The results of CO and H_2 obtained with non-unity *Le* are shown in Fig. 11. It is seen that the two species are much better predicted. Better prediction of hydrogen with non-unity *Le* is expected, since *Le* of H_2 is much smaller than unity (around 0.3). However, the non-unity *Le* appears essential for CO as well, although the *Le* of CO is very close to unity. Han et al. [24] also reproduced the CO by using detailed transport properties in the LES of a premixed jet ame. With the present results, the importance of detailed transport properties for the CO prediction can be highlighted.

Similar to Fig. 9, effects of *Le* and ϕ on the equilibrium CO and H_2 are shown in Fig. 12. Equilibrium mass fractions of CO and H_2 increase with ϕ. In Fig. 9(a), CO_2 decreases with $\phi > 1$, which should result from a reduced oxidation of CO at richer conditions.

From Fig. 8c, the augmented equivalence ratio in the IRZ attains even $\phi = 1.1$. The increase of CO and H_2 mass fractions in the laminar flames from $\phi = 1.0$ to 1.1 is shown in Fig. 12. It can be seen that the mass fraction increments in Fig. 12 are almost equivalent to that in Fig. 11 (at $z = 10$ mm). Therefore, the improved
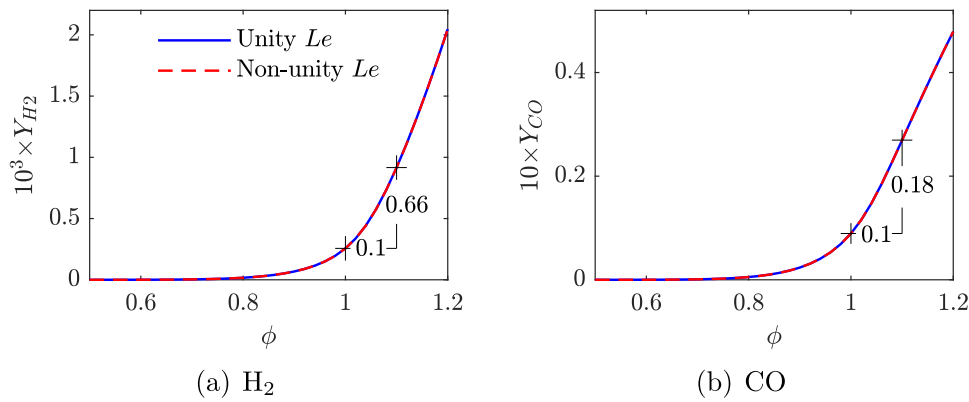
Fig. 12. Influence of Le and ϕ on the equilibrium mass fractions of CO and H_2.

predictions of CO and H_2 in Fig. 11 are expected to be mainly caused by the increased ϕ with non-unity Le. With unity Le, CO and H_2 are under-predicted because the increased ϕ can not be captured. The higher ϕ predicted by case ZZ2PV-Le with stretch leads to slightly improved CO and H_2 predictions in Fig. 11. But it only plays a minor role, since CO and H_2 are well reproduced overall even without stretch effects in the manifold. RMS results of the two species are shown in Appendix B.

Accordingly, one previous conclusion that the under-predicted CO is due to the over-predicted temperature can be corrected [1,6]. The higher temperature is merely another consequence of the increased ϕ. It needs to be addressed that, the slow oxidation rate of CO is not the main cause of the under-prediction, as mentioned in [36,49], since with unity Le, the transported CO can not improve its prediction significantly (Fig. 10). With non-unity Le, the tabulated value of CO is accurate enough.

4. Conclusions

Non-adiabatic LES-FGM simulations for the Cambridge/Sandia stratified flame (SwB5) were performed. The influence of reduced and detailed transport properties was investigated by comparing the results of two FGM manifolds with unity and non-unity Le, respectively. Stretch effects were examined by using another manifold tabulated with stretched flamelets. Satisfactory agreement was found between simulation and experimental results of the velocity fields, species mass fraction, equivalence ratio ϕ and temperature. The main conclusions are as follows:

1) The inclusion of non-unity Le and stretch shows nearly no effect on the velocity statistics. Most of the scalars can be well predicted with a unity Le assumption, except for CO, H_2 and ϕ in the IRZ.
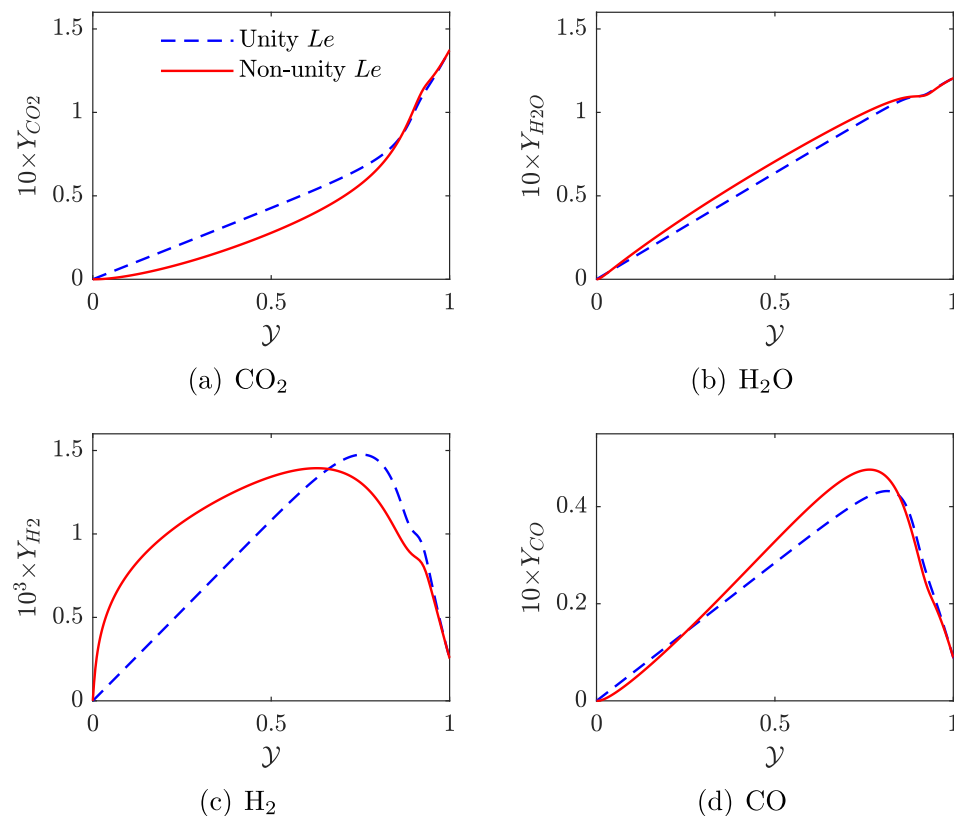

Fig. A13. Effect of Le on the species mass fractions in the adiabatic laminar flames ($\phi = 1.0$, T_u=300 K).
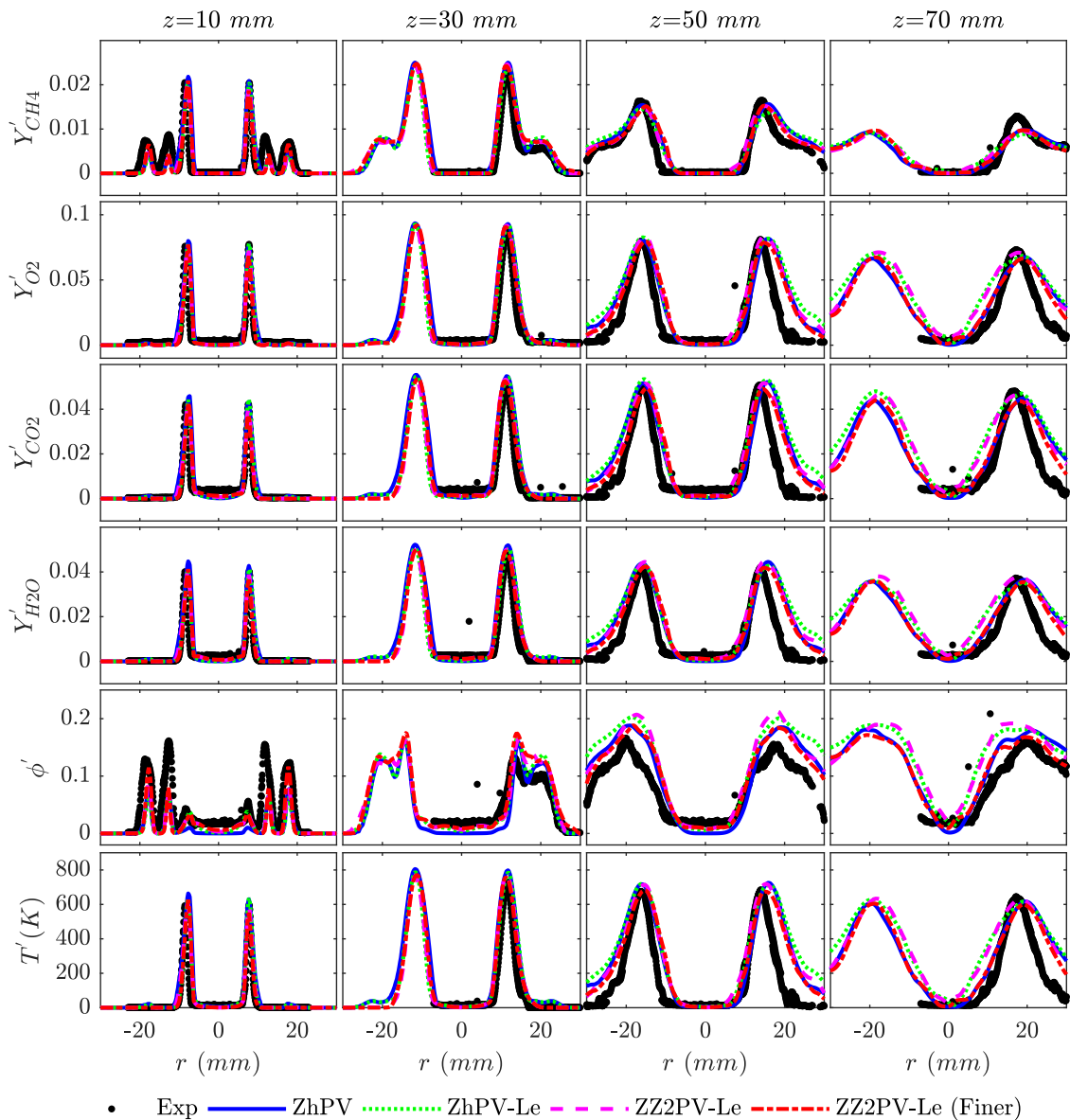
Fig. B.14. RMS results of the scalars of all the simulated cases.

2) With non-unity *Le*, the experimentally measured higher ϕ in the IRZ can be reproduced. It can not be captured with unity *Le*. Meanwhile, inclusion of stretch further increases the simulated ϕ in the IRZ.

3) However, with non-unity *Le*, the simulated high ϕ deteriorates the near-wall temperature modeling even with heat loss. With stretch, the prediction can be improved even without heat loss. The high ϕ also leads to deviations of equilibrium CO_2 and H_2O in the IRZ.

4) It is proposed that accounting for non-unity *Le* is crucial for both H_2 and CO predictions. This mainly benefits from the well reproduced ϕ. With unity *Le*, an additional transport equation will not significantly improve the CO prediction, which indicates that the slow oxidation of CO is not the main problem.

5) Stretch is found to slightly improve the major species and temperature predictions except for CO_2 and H_2O in the IRZ, due to its contribution to the increased ϕ there.

Based on this study, the equivalence ratio (or mixture fraction *Z*) modeling seems very important, since several non-unity *Le* ef-

fects can all be explained by the increased ϕ especially in the IRZ. Note that it should not be enough to only calculate the flamelets with non-unity *Le*. The Lewis number effects also need to be accounted for in the transport equations of the CVs to predict better results, as performed in this study. With non-unity *Le*, although the equivalence ratio, H_2 and CO predictions are evidently improved, the near-wall temperature, CO_2 and H_2O are deteriorated (but not too seriously). The underlying reason is that the FGM may not capture all the physical-chemical-thermal processes as a reduced model. A more complete model to include all the heat loss (also radiation), preferential diffusion and stretch effects, etc., is expected to further improve the results. This remains to be explored in the future.

Declaration of Competing Interest

The authors declare that they have no known competing financial interests or personal relationships that could have appeared to influence the work reported in this paper.
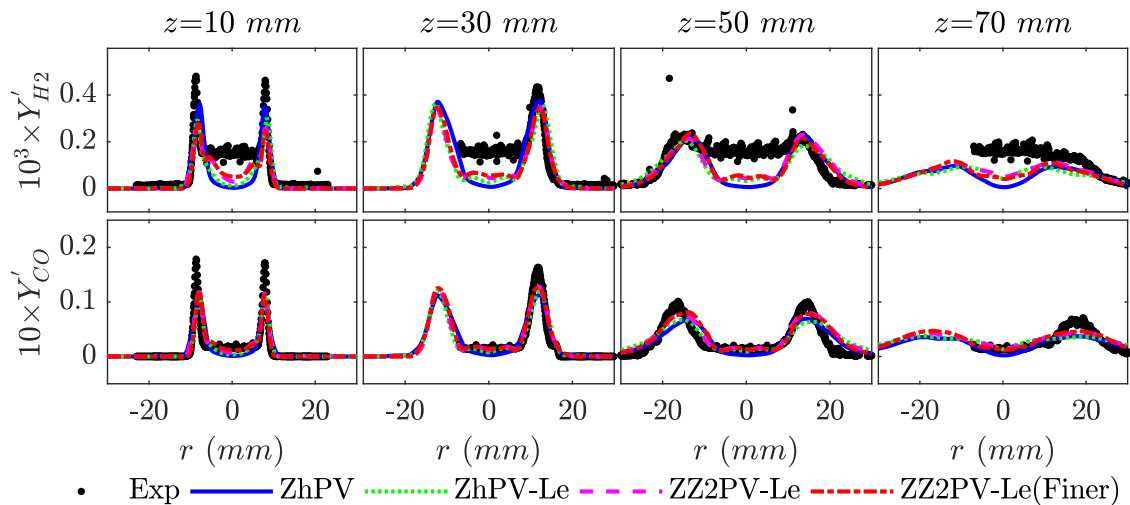
Fig. B.15. RMS results of CO and H₂.

Appendix A. Species mass fractions in the flamelet

Please see Fig. A.13, the species production can be modified by non-unity Le within the laminar flamelets. However, it shows no effects on the equilibrium mass fraction of the species (around $\mathcal{Y} = 1$).

Appendix B. RMS results of the scalars

Please see Fig. B.14, rms results of the scalars are well predicted except for in the downstream region, probably due to a larger unresolved SGS term. The asymmetric error still appears for the experimental results. Meanwhile, rms result of the equivalence ratio is slightly under-predicted.

RMS results of CO and H₂ mass fraction are shown in Fig. B.15. The result of CO is well predicted whereas some deviations appear for H₂ when $r \to 0$.

References

[1] H. Turkeri, X. Zhao, S.B. Pope, M. Muradoglu, Large eddy simulation/probability density function simulations of the Cambridge turbulent stratified flame series, Combust. Flame 199 (2019) 24–45.

[2] A. Masri, Partial premixing and stratification in turbulent flames, Proc. Combust. Inst. 35 (2) (2015) 1115–1136.

[3] A.N. Lipatnikov, Stratified turbulent flames: recent advances in understanding the influence of mixture inhomogeneities on premixed combustion and modeling challenges, Prog. Energy Combust. Sci. 62 (2017) 87–132.

[4] M.S. Sweeney, S. Hochgreb, M.J. Dunn, R.S. Barlow, The structure of turbulent stratified and premixed methane/air flames I: non-swirling flows, Combust. Flame 159 (9) (2012) 2896–2911.

[5] M.S. Sweeney, S. Hochgreb, M.J. Dunn, R.S. Barlow, The structure of turbulent stratified and premixed methane/air flames II: swirling flows, Combust. Flame 159 (9) (2012) 2912–2929.

[6] F. Proch, A.M. Kempf, Numerical analysis of the Cambridge stratified flame series using artificial thickened flame LES with tabulated premixed flame chemistry, Combust. Flame 161 (10) (2014) 2627–2646.

[7] S. Nambully, P. Domingo, V. Moureau, L. Vervisch, A filtered-laminar-flame PDF sub-grid scale closure for LES of premixed turbulent flames. Part I: formalism and application to a bluff-body burner with differential diffusion, Combust. Flame 161 (7) (2014) 1756–1774.

[8] S. Nambully, P. Domingo, V. Moureau, L. Vervisch, A filtered-laminar-flame PDF sub-grid-scale closure for LES of premixed turbulent flames: II. Application to a stratified bluff-body burner, Combust. Flame 161 (7) (2014) 1775–1791.

[9] R. Mercier, T. Schmitt, D. Veynante, B. Fiorina, The influence of combustion SGS submodels on the resolved flame propagation. Application to the LES of the Cambridge stratified flames, Proc. Combust. Inst. 35 (2) (2015) 1259–1267.

[10] T. Brauner, W. Jones, A. Marquis, LES of the Cambridge stratified swirl burner using a sub-grid PDF approach, Flow Turbul. Combust. 96 (4) (2016) 965–985.

[11] R.S. Barlow, M.J. Dunn, M.S. Sweeney, S. Hochgreb, Effects of preferential transport in turbulent bluff-body-stabilized lean premixed CH4/air flames, Combust. Flame 159 (8) (2012) 2563–2575.

[12] V. Katta, W.M. Roquemore, C/H atom ratio in recirculation-zone-supported premixed and nonpremixed flames, Proc. Combust. Inst. 34 (1) (2013) 1101–1108.

[13] C. Law, C. Sung, Structure, aerodynamics, and geometry of premixed flamelets, Prog. Energy Combust. Sci. 26 (4–6) (2000) 459–505.

[14] A. Donini, R. Bastiaans, J. van Oijen, L. De Goey, Differential diffusion effects inclusion with flamelet generated manifold for the modeling of stratified premixed cooled flames, Proc. Combust. Inst. 35 (1) (2015) 831–837.

[15] J. Van Oijen, A. Donini, R. Bastiaans, J. ten Thije Boonkkamp, L. De Goey, State-of-the-art in premixed combustion modeling using flamelet generated manifolds, Prog. Energy Combust. Sci. 57 (2016) 30–74.

[16] P. Venkateswaran, A. Marshall, J. Seitzman, T. Lieuwen, Scaling turbulent flame speeds of negative Markstein length fuel blends using leading points concepts, Combust. Flame 162 (2) (2015) 375–387.

[17] W. Zhang, J. Wang, W. Lin, R. Mao, H. Xia, M. Zhang, Z. Huang, Effect of differential diffusion on turbulent lean premixed hydrogen enriched flames through structure analysis, Int. J. Hydrog. Energy 45 (18) (2020) 10920–10931.

[18] A. Vreman, J. Van Oijen, L. De Goey, R. Bastiaans, Direct numerical simulation of hydrogen addition in turbulent premixed bunsen flames using flamelet-generated manifold reduction, Int. J. Hydrog. Energy 34 (6) (2009) 2778–2788.

[19] J.B. Bell, R.K. Cheng, M.S. Day, I.G. Shepherd, Numerical simulation of lewis number effects on lean premixed turbulent flames, Proc. Combust. Inst. 31 (1) (2007) 1309–1317.

[20] A. Aspden, M. Day, J. Bell, Turbulence–flame interactions in lean premixed hydrogen: transition to the distributed burning regime, J. Fluid Mech. 680 (2011) 287–320.

[21] M. Day, J. Bell, P.-T. Bremer, V. Pascucci, V. Beckner, M. Lijewski, Turbulence effects on cellular burning structures in lean premixed hydrogen flames, Combust. Flame 156 (5) (2009) 1035–1045.

[22] R. Mercier, C. Mehl, B. Fiorina, V. Moureau, Filtered wrinkled flamelets model for large-eddy simulation of turbulent premixed combustion, Combust. Flame 205 (JUL.) (2019) 93–108.

[23] C. Mehl, M. Cailler, R. Mercier, V. Moureau, B. Fiorina, Optimized chemistry for large eddy simulations of wrinkled flames, Proc. Combust. Inst. (2020) 1–10, doi:10.1016/j.proci.2020.09.028. JUL.

[24] W. Han, H. Wang, G. Kuenne, E.R. Hawkes, J.H. Chen, J. Janicka, C. Hasse, Large eddy simulation/dynamic thickened flame modeling of a high Karlovitz number turbulent premixed jet flame, Proc. Combust. Inst. 37 (2) (2019) 2555–2563.

[25] J. Van Oijen, R. Bastiaans, L. de Goey, Modelling preferential diffusion effects in premixed methane-hydrogen-air flames by using flamelet-generated manifolds, Fifth European Conference on Computational Fluid Dynamics (2010). Lisbon, Portugal

[26] E. Knudsen, H. Kolla, E.R. Hawkes, H. Pitsch, LES of a premixed jet flame DNS using a strained flamelet model, Combust. Flame 160 (12) (2013) 2911–2927.

[27] J. Van Oijen, R. Bastiaans, L. De Goey, Low-dimensional manifolds in direct numerical simulations of premixed turbulent flames, Proc. Combust. Inst. 31 (1) (2007) 1377–1384.

[28] J. Van Oijen, L. De Goey, Modelling of premixed counterflow flames using the flamelet-generated manifold method, Combust. Theor. Model. 6 (3) (2002) 463–478.

[29] J. Van Oijen, L. De Goey, Modelling of premixed laminar flames using flamelet–generated manifolds, Combust. Sci. Technol. 161 (1) (2000) 113–137.

[30] J.A. van Oijen, Flamelet-Generated Manifolds: Development and Application to Premixed Laminar Flames, Technische Universiteit Eindhoven, Eindhoven, 2002.

[31] J.A. de Swart, R.J. Bastiaans, J.A. van Oijen, L.P.H. de Goey, R.S. Cant, Inclusion of preferential diffusion in simulations of premixed combustion of hydrogen/methane mixtures with flamelet generated manifolds, Flow Turbul. Combust. 85 (3–4) (2010) 473–511.

[32] P. Trisjono, K. Kleinheinz, H. Pitsch, S. Kang, Large eddy simulation of stratified and sheared flames of a premixed turbulent stratified flame burner using a flamelet model with heat loss, Flow Turbul. Combust. 92 (1–2) (2014) 201–235.

[33] B. Fiorina, R. Mercier, G. Kuenne, A. Ketelheun, A. Avdić, J. Janicka, D. Geyer, A. Dreizler, E. Alenius, C. Duwig, et al., Challenging modeling strategies for les of non-adiabatic turbulent stratified combustion, Combust. Flame 162 (11) (2015) 4264–4282.

[34] R. Zhou, S. Balusamy, M.S. Sweeney, R.S. Barlow, S. Hochgreb, Flow field measurements of a series of turbulent premixed and stratified methane/air flames, Combust. Flame 160 (10) (2013) 2017–2028.

[35] E. Fedina, C. Fureby, G. Bulat, W. Meier, Assessment of finite rate chemistry large eddy simulation combustion models, Flow Turbul. Combust. 99 (2) (2017) 385–409.

[36] A. Donini, R. Bastiaans, J. van Oijen, L. de Goey, A 5-D implementation of FGM for the large eddy simulation of a stratified swirled flame with heat loss in a gas turbine combustor, Flow Turbul. Combust. 98 (3) (2017) 887–922.

[37] R. Bilger, The structure of turbulent nonpremixed flames, Proc. Combust. Inst. 22 (1) (1989) 475–488.

[38] Chem1D, A One-Dimensional Laminar Flame Code, Eindhoven University of Technology, 2016.

[39] G.P. Smith, D.M. Golden, M. Frenklach, N.W. Moriarty, B. Eiteneer, M. Goldenberg, C.T. Bowman, R.K. Hanson, S. Song, W.C. Gardiner Jr, et al., GRI 3.0 Mechanism, Gas Research Institute, 1999. (http://www.me.berkeley.edu/gri_mech).

[40] A. Ketelheun, G. Kuenne, J. Janicka, Heat transfer modeling in the context of large eddy simulation of premixed combustion with tabulated chemistry, Flow Turbul. Combust. 91 (4) (2013) 867–893.

[41] A. Donini, Advanced turbulent combustion modeling for gas turbine application (2014).

[42] A. Vreman, B. Albrecht, J. Van Oijen, L. De Goey, R. Bastiaans, Premixed and nonpremixed generated manifolds in large-eddy simulation of Sandia flame d and f, Combust Flame 153 (3) (2008) 394–416.

[43] J. Floyd, A.M. Kempf, A. Kronenburg 1, R. Ram, A simple model for the filtered density function for passive scalar combustion LES, Combust. Theor. Model. 13 (4) (2009) 559–588.

[44] C.D. Pierce, P. Moin, A dynamic model for subgrid-scale variance and dissipation rate of a conserved scalar, Phys. Fluids 10 (12) (1998) 3041–3044.

[45] C. Olbricht, O. Stein, J. Janicka, J. Van Oijen, S. Wysocki, A. Kempf, LES of lifted flames in a gas turbine model combustor using top-hat filtered PFGM chemistry, Fuel 96 (2012) 100–107.

[46] B. Fiorina, R. Vicquelin, P. Auzillon, N. Darabiha, O. Gicquel, D. Veynante, A filtered tabulated chemistry model for LES of premixed combustion, Combust. Flame 157 (3) (2010) 465–475.

[47] M. Klein, A. Sadiki, J. Janicka, A digital filter based generation of inflow data for spatially developing direct numerical or large eddy simulations, J. Comput. Phys .186 (2) (2003) 652–665.

[48] M.C. Immer, Time-Resolved Measurement and Simulation of Local Scale Turbulent Urban Flow, ETH Zurich, 2016 Ph.D. thesis.

[49] A. Ketelheun, C. Olbricht, F. Hahn, J. Janicka, No prediction in turbulent flames using LES/FGM with additional transport equations, Proc. Combust. Inst. 33 (2) (2011) 2975–2982.